256-channel magnetic imaging system

F. C. S. da Silva
University of Colorado Denver, Denver, Colorado, 80217-3364, USA

S. T. Halloran, A. B. Kos, and D. P. Pappas
National Institute of Standards and Technology, Boulder, Colorado 80305, USA

(Received 13 September 2007; accepted 7 December 2007; published online 18 January 2008)

We present the design and fabrication of a magnetoresistive imaging system capable of scanning 256 channels simultaneously along linear ranges of either 4 or 13 mm. High speed electronics read the channels and transfer the data to a computer that builds and displays the images. The system was successfully used to image magnetic tapes for real-time forensic validation purposes and can also be applied in other noninvasive imaging applications. © *2008 American Institute of Physics.*
[DOI: 10.1063/1.2829883]

I. INTRODUCTION

Imaging the fields generated by magnetic media, e.g., magnetic audio or video tapes, is critical to validating evidence in criminal investigation analyses.[1] The Bitter technique is the conventional way to conduct this analysis.[2] In this method the examiner uses a solution containing solvent and magnetic particles to coat the evidence tape. After the solvent is evaporated, the particles accumulate in areas where the magnetization of the tape changes direction. These areas produce strong field gradients in the direction perpendicular to the tape surface [Fig. 1(a)] and therefore attract the magnetic particles. The examiner observes the particle distribution at the tape surface with an optical microscope.

When implementing the Bitter technique as a forensics tool, it is important to use solutions that can be completely cleaned from the evidence. This limits examiners to the use of relatively large magnetic particles, thereby reducing the spatial resolution of the image. In addition, because the Bitter technique is not sensitive to the polarity of the transition, it is impossible to decode the information. Finally, this technique has a small field of view and is extremely time consuming. It requires examiners to extract the tape, develop the fluid, find the specific event of interest, image it, and clean the evidence. Figure 1(b) shows an image obtained using the Bitter technique. The image is of a 400 Hz stereo-sine-wave recorded on the top half of a cassette tape and a monorecording of a recording head stop event on the bottom half of the tape.

In a recent publication, Pappas *et al.*[3] proposed a novel alternative to the Bitter technique that is noninvasive, sensitive to field polarity, has high spatial resolution, and has the potential to make images as the tape is played. The technique uses a magnetoresistive (MR) scanning head commonly employed in magnetic hard drives [Fig. 1(c)]. The head scans across the surface of the magnetic tape to produce high-resolution images. Figure 1(d) shows a MR-head image scan of the same tape used in Fig. 1(b). In this image, we see an improved contrast, spatial resolution, and the polarity of the sine-wave signal.

Despite the improvements, the scanning head technique has many of the same limitations of the Bitter technique, e.g., manual extraction of the tape, small field of view, and long acquisition time. However, the potential for scalability and integration of the scanning head technique associated with fast multichannel data acquisition systems facilitated the development of a real-time magnetic scanner.

II. DESCRIPTION

In this paper we present the design and fabrication of a high speed, real-time magnetoresistive imaging system capable of measuring 256 channels per scan with either a 4 or 13 mm wide device at an acquisition rate of 8 kscans/s. The host computer controls the acquisition, displays the images, and tracks the corresponding audio signature of any channel in real time. The system can image magnetic tapes for forensic validation purposes and can furthermore be applied in other noninvasive imaging applications such as imaging current paths in printed circuit boards and integrated circuits.

A photograph of the tape scanning apparatus is shown in Fig. 2. The system uses a modified tape transport from a commercial player. The tape is extracted and passes over both the player head as well as the 256-channel magnetoresistive head. We have developed scanning systems that can image either audio (4 mm wide) or video cassette (13 mm wide) tapes. The heads are interfaced to the preamplifier board via a grid array of spring-loaded pins housed in a socket that provides mechanical pressure for electrical contacts and head alignment. The system is automated by a computer that controls the audio tape player and the multichannel head transport into the tape path while it is playing. Calibration of the head is also automated using linear servomotors to move the head over a calibration coil.

A schematic diagram of the system is shown in Fig. 3. Here, the audio tape player or the video tape player interfaces directly with the 256 sensors in the array. The sensor signals are channeled in 16 groups of 16 channels by a multiplexer (mux.) Each group of 16 channels is transferred to an amplifier box and digitized by two eight-channel analog-

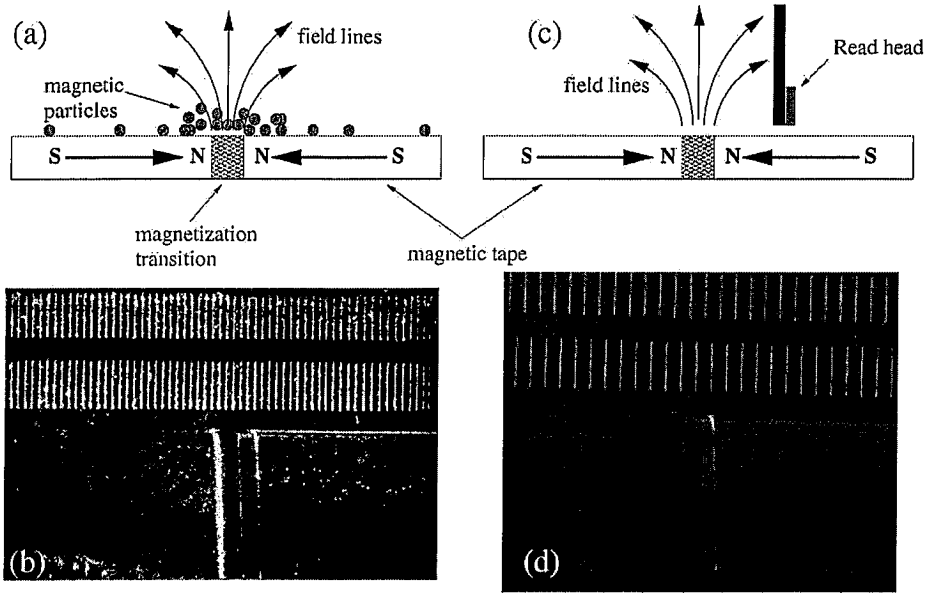

FIG. 1. Comparison between the Bitter technique [(a) and (b)] and the scanning read head technique [(c) and (d)]. The diagrams illustrate the principle of operation for the (a) Bitter and (c) read head techniques. The images show the results obtained by scanning the same tape using the (b) Bitter and (d) read head techniques.

to-digital converters (ADCs) placed inside the host computer. The ADCs digitize 16 channels in 5 μs or all 256 channels in 80 μs. By defining one scan as 256 channels, the maximum nominal update rate is therefore 12.5 kscans/s. Power for the sensor array is provided by a power supply integrated into the amplifier box.

III. SENSOR ARRAY

The core of the magnetic imaging system is the MR sensing element. The MR element maps the amplitude of the magnetic field into a resistance value. The proper operation of a MR sensor depends on several factors. In general, within the range of operation, the MR element should have a linear magnetic response, be hysteresis free, have a dynamic range that is compatible with the measurement requirements, have low noise at low frequencies, and be able to recover from spikes in temperature and magnetic field. For arrays of MR sensors, additional features such as cross-talk noise (electric and magnetic,) repeatability tolerances, yield, and common mode rejection (thermal, electric, and magnetic) need to be optimized for proper operation.

To ensure the success of this project, we chose sensing elements based on the anisotropic magnetoresistive (AMR) effect for a number of key reasons. First, in order to reject thermal asperities and have a low common mode voltage, it is necessary to build multiple four-element bridges that have an asymmetric response to the applied magnetic field and are well balanced. AMR elements satisfy these requirements because (1) the relative slope of the transfer curves of each element in the bridges can be set by the symmetry of the contacts, and (2) both the magnetic layer (NiFe) and contact layer (Al) can be obtained in single deposition steps for all elements. This avoids unbalanced bridges, thereby allowing for high gain and dynamic range. For other types of MR sensors, i.e., giant and tunneling magnetoresistors, it would be necessary to set the pinning layers for the bridge elements in different directions using multiple deposition steps or other more complicated biasing methods. Secondly, because AMR sensors use only one magnetic layer, they have much lower noise at low frequency (up to an order of magnitude better) than the other types of MR sensors.

Finally, new research has shown that it is possible to

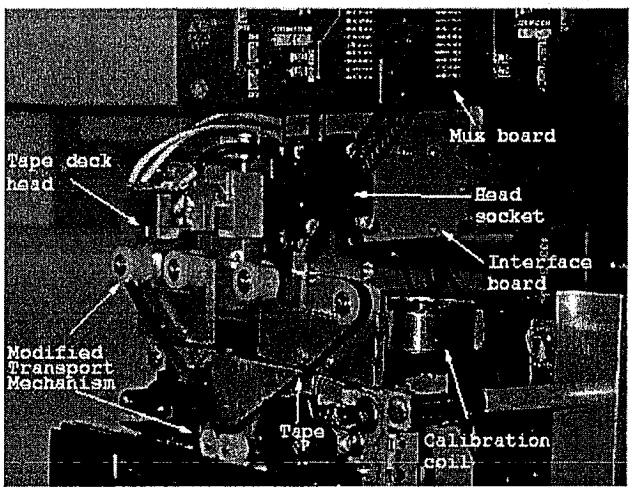

FIG. 2. (Color online) Photograph of the transport mechanism used in the imaging of audio tapes.

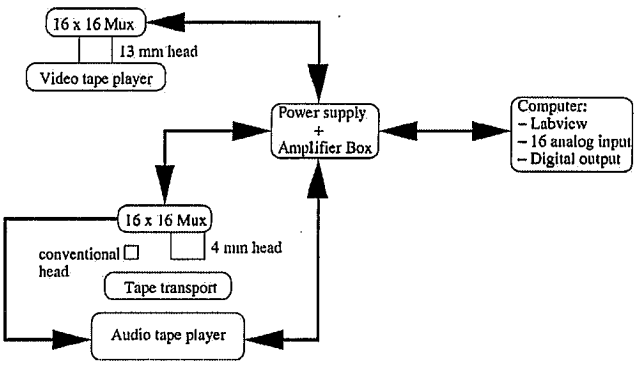

FIG. 3. Schematic diagram of the imaging system.

adjust the sensitivity and dynamic range of AMR sensors using an antiferromagnetic pinning layer that is weakly coupled to the sense layer with a thin metallic film (in this case Ru).[4] This layer also maintains the direction and magnetization of the free layer, making it unnecessary to use a set/reset strap.[5] Therefore, we retain all of the advantages of the AMR sensors with increased dynamic range and stability.

Other advantages of AMR sensors are that they are more resistant to electrostatic discharges and are scalable to submicrometer lengths (e.g., dual-stripe technology).[5] This means that the potential linear density of this system could be 10^4 channels in 4 mm. At present, the density is limited to 256 sensors/ 4 mm by the geometry constraints of the interconnections. This constraint could be lifted by integrating the sensors with a complementary metal oxide semiconductor front end (preamp and multiplexer) in the Si wafer.[6] The remainder of this section is devoted to an itemized description of the sense element design and how they address the design rules.

A. Sensing element structure

The magnetic sensing element is composed of an AMR layer biased along the easy axis by a tunable exchange-bias multilayer structure.[4,7] The exchange-bias effect, normally attributed to a ferromagnet-antiferromagnet (FM-AFM) interface,[8] is tuned by placing a nonmagnetic spacer with adjustable thickness between the FM and AFM layers.

The optimum bias should maximize the easy-axis hysteresis loop shift and the slope of the hard-axis loop (Fig. 4.) However, the hysteresis loop shift and the hard-axis loop slope have a reciprocal correspondence because a reduction in sensitivity will always occur for higher exchange-bias shifts in the hysteresis curve. As a general design rule, we try to find the minimum exchange-bias shift that removes the hysteresis in the remanent state.

Figure 4 shows the behavior of the exchange-bias shift and the slope of the hard-axis loop for different values of the Ru spacer thickness t in comparison to a sample with no exchange bias. The easy-axis loops in Figs. 4(a)–4(c) show that for increasing values of t, the exchange-bias shift decreases and that the hysteresis curve approaches the no-bias curve limit for $t>1$ nm. Similarly, the slope of the hard-axis loop increases for increasing values of t. A good compromise between these two parameters is $t=0.5$ nm where the remanent state is nonhysteretic and the slope of the hard-axis loop is not significantly smaller than that of the no-bias sample. Here, the measured shift in the hysteresis curve is 850 A m^{-1}.

The detailed structure of the sensing element (Fig. 5) starting from the bottom is Ta (3 nm)/Ru (8 nm)/IrMn (8 nm)/Ru (0.5 nm)/$Ni_{81}Fe_{19}$ (22 nm)/Ta (3 nm). The bottom layers of Ta and Ru are, respectively, for adhesion to the thermally oxidized Si substrate and texturing the IrMn. The IrMn layer provides a stable antiferromagnetic exchange bias, while the second Ru layer reduces the bias to an optimal value. The AMR sense layer is next, composed of a $Ni_{81}Fe_{19}$ film deposited in a 16 kA m^{-1} field along the easy-axis direction. Finally, the top Ta layer protects the AMR layer against oxidation. The substrate is a thermally oxidized

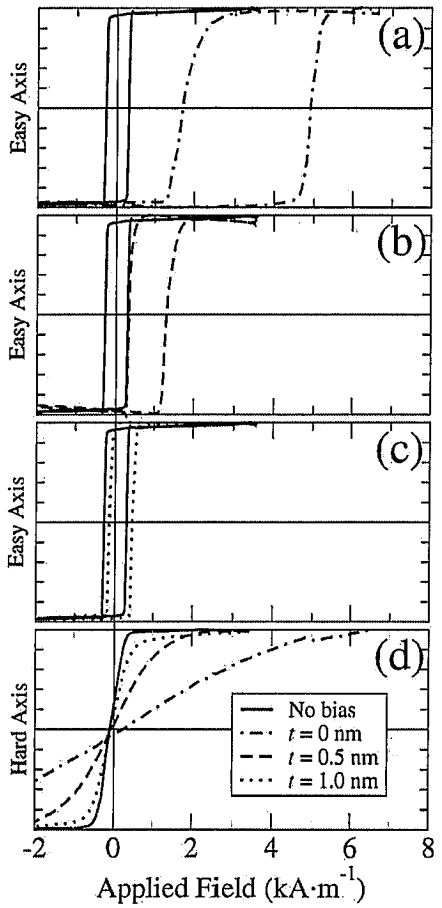

FIG. 4. Normalized hysteresis loops showing a comparison between samples prepared with different thicknesses t of the Ru spacer (dotted lines) and the no exchange-bias sample (solid lines.) The dotted lines in the easy-axis loops [(a)–(c)] correspond to t=0, 0.5, and 1.0 nm, respectively. The hard-axis loops are shown in (d).

(100) Si wafer with a 150 nm oxide layer. The structure is deposited on a lift-off resist patterned wafer and hysteresis curves for the easy and hard axes are measured prior to the lift-off step.

The sensing element geometry is also shown in Fig. 5. Here we chose a needle-shaped element of 12.5 μm in length and 2 μm wide for the audio tape head and 43 μm in length and 2 μm wide for the video tape head. The effective lateral or cross-track spatial resolutions of the array are

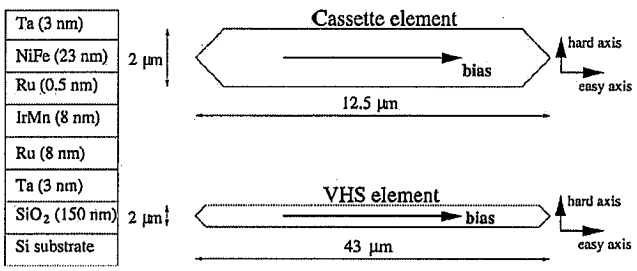

FIG. 5. Schematic side view of the multilayered structure of the sensing element (left) and the top view geometry of the sensing element for the cassette (top right) and video (bottom right) sensor array. The bias shown is from the antiferromagnet pinning layer.

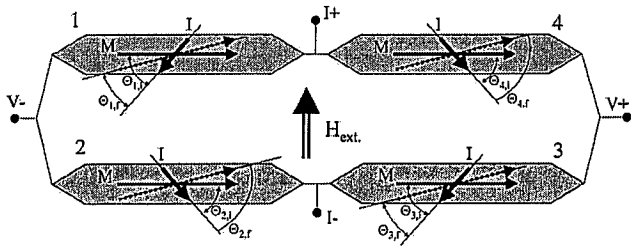

FIG. 6. Schematic view of bridge built with AMR elements with the current biased at 45°. The long, solid arrows represent the magnetization in an initial zero field (*i*), and the dotted arrows illustrate the rotation of the magnetization in the final field (*f*), H_{ext}. The short arrows show the current direction, defined by the barber pole shorting lines on top of the AMR elements.

16 μm for the audio tape head and 48 μm for the video tape head.

The magnetic response of the elements is the most important aspect of the design. The sensing elements are designed with the unidirectional anisotropy maintaining a relatively uniform magnetization in the active central region. As mentioned before this was achieved using both the exchange bias through the Ru spacer to the antiferromagnetic layer and the dipole energy (due to the high aspect ratio) of the element. The anisotropy field H_k, which sets the sensitivity of the magnetization to the applied field, was adjusted with the thickness of the Ru spacer and adjusting the aspect ratio.[4]

The resistance change of the AMR elements in a magnetic field, i.e., the transfer curve, and the design of devices based on this effect are well known.[5] In the AMR effect, the resistance change is given by $\delta R \propto \cos^2(\theta)$, where θ is the angle between the current and the magnetization. This results in a high resistance when the two are collinear, and a low resistance when they are perpendicular to each other, i.e., $\theta = 0$ and 90°, respectively. The signal is therefore linearized by biasing the absolute value of θ to ±45°. In this implementation, we use the barber pole configuration to bias the current in the element. This is achieved with equipotential shorting bars (barber poles) on top of the magnetic element. The unique aspect of the AMR barberpole design is that the slope of the transfer curve is set by the relative angle of the current versus the magnetization. Therefore, a Wheatstone bridge configuration can be set up by designing the shorting bars at ±45°. This is illustrated in Fig. 6. When a homogeneous magnetic field $\mathbf{H}_{ext}$ is applied, the angles decrease for elements 1 and 3, while the angles increase for elements 2 and 4. This decreases/increases the resistances, respectively, thereby unbalancing the bridge.

This design allows us to deposit and pattern all of the magnetic elements in a single step because the magnetization is in the same direction on all of the elements. The contact layer, with barber pole shorting bars, can then be deposited and patterned in another single step. Thus, we can maintain the high level of homogeneity in the structures to ensure that the bridges are well balanced. In addition, the barber pole patterns are designed to reduce the effects of misalignment between the layers. Finally, by setting the slopes of alternating bridges, we are able to assemble a network that can be stepped through sequentially.

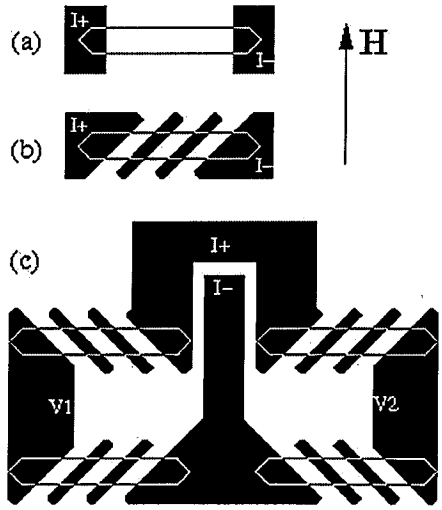

FIG. 7. To-scale physical layout diagram of the test structures fabricated on idle areas of the sensor array: (a) Single element, (b) single barber pole, and (c) barber pole bridge. The sensed magnetic field **H** is perpendicular to the long axis of the sensing elements.

B. Magnetotransport properties

Because the fabrication involves many steps and a comprehensive system check can only be performed after the last stage of the process, test devices were designed in unused areas of the sensor chip. These devices, measured after the third metallization layer step, provided the magnetoresistive response of the sensing elements in three configurations. The configuration shown in Fig. 7(a) gives information about the basic operation of the magnetic layer. The diagram shown in Fig. 7(b) tests the barber pole response of a single element. Finally the bridge configuration in Fig. 7(c) tests the full bridge design described above.

Figure 8(a) shows the hard-axis AMR response for a single element without the barber poles. In this configuration, the resistance traces an inverted parabolic shape versus the external applied field. From these data and assuming the sensing element acts as a single-domain particle, we estimate a bias field of $H_b = 12.5$ kA m^{-1} for the patterned elements. This is higher than the value measured at the wafer level. The increase reflects the difference in magnetostatic (dipole) energy between the single element and the unpatterned film.

Figure 8(b) shows the transfer curve of a test device with contacts for the barber pole configuration. This is the main building block of the sensor bridge. In this configuration, the barber pole lines linearize the magnetic field response around zero field. This is accomplished by orienting the lines at a 45° angle with respect to the long axis of the sensing element. By using aluminum, which is much more conductive than $Ni_{81}Fe_{19}$, the barber pole lines will bias the direction of the current inside the AMR layer at approximately the same angle.

By combining four barber pole AMR elements in a bridge configuration as shown in Figs. 6 and 7(c), the sensing cell produces a symmetric response to the magnetic field [see Fig. 8(c)]. On each leg of the bridge, two barber pole sensing elements with current bias angles of +45° and −45° (± for simplicity) produce twice the resistance change of a

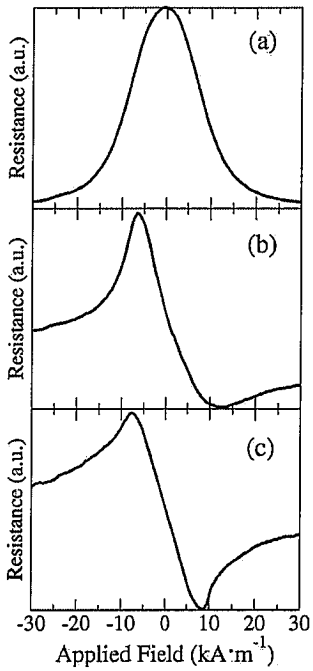

FIG. 8. Experimental magnetoresistance curves measured for the (a) single element, (b) single barber pole, and (c) barber pole bridge as a function of the external applied field as described in Fig. 7.

single element. The bias sequence on each leg alternates ($\pm$ and $\mp$) in order to provide a differential signal that is proportional to the applied field. This bridge configuration rejects first-order thermal, electrical, and magnetic common modes.

The thermal common mode rejection comes from the proximity of the sensors to each other and how fast heat propagates in the system. Finite element analysis simulations show that 100 K temperature spikes above the background occurring 4 μm from the edge of the sensors are sensed by the two elements (5.5 μm apart) in less than 10 μs. These conditions simulate a thermal asperity and hence limits the maximum acquisition rate to 50 kHz according to Nyquist's theorem.

Finally, the intrinsic electrical and magnetic noise of the sensors is about 20 nT/$\sqrt{\text{Hz}}$. Given that the sampling bandwidth is 250 kHz, we expect a noise floor of the system of 0.01 mT for a perfectly balanced bridge. With standard dies, the system is able to regularly achieve 0.1 mT resolution. This gives a signal to noise ratio of about 100:1 for erase head events on typical magnetic tape media. Therefore, we find that the bridge design using AMR barber pole sensors is critical to the operation of the sensor array because it measures the magnetic signal with a tunable dynamic range and provides suitable rejection of the main sources of offsets, drift, and noise.

C. Fabrication

The fabrication of the sensor array uses standard patterning, deposition, and etching processes. The specific choice of process and layout rules used here depended on the level of component integration, critical feature size, and repeatability of the pattern that ultimately affects the yield of each channel of the array. We designed and fabricated 14 masks using a 1 μm resolution pattern generator and chrome-coated soda-lime plates. Table I describes the process steps.

TABLE I. Processes involved in the fabrication of the sensor array. The first column describes the individual lithographic steps. If the step is a deposition, the second column shows the deposited material and in parenthesis the deposition method. If the step requires an etch, the third column shows the etch method. The fourth column indicates whether the step is a lift-off step or not.

Step	Depositions	Etches	Lift-offs
Alignment marks	None	RIE	None
Power plane 1	Al (sputtering)	Wet	None
AMR layer	Ta/Ru/IrMn/Ru/NiFe/Ta (sputtering)	None	Yes
AMR contacts	Al (e-beam)	None	Yes
Via 1	SiO_2 (CVD)	RIE	None
Power plane 2	Al (sputtering)	Wet	None
Via 2	SiO_2 (CVD)	RIE	None
Contact 1	Al (sputtering)	Wet	None
Via 3	SiO_2 (CVD)	RIE	None
Contact 2	Al (sputtering)	Wet	None
Via 4	SiO_2 (CVD)	RIE	None
Platting	Ti/AuPd (e-beam)	None	Yes
Dicing	None	DRIE	None

The metallic layers were deposited using sputtering and electron-beam evaporation. The SiO_2 insulating layers, deposited by plasma enhanced chemical vapor deposition (CVD), provided a conformal coating of the metallic layers and low density of pinholes in the oxide.

Two dry-etch methods were used in the fabrication: a regular reactive ion etch (RIE) for the insulator layer and a deep reactive ion etch (DRIE) for cutting an edge line on the Si wafer of 4 μm from the linear sensor array. The sputter-deposited Al layers were etched using an alkaline etching solution. Ar plasma or ion-mill cleaning steps were performed before each deposition.

The patterning exposure used an I-line stepper in two types of positive resist and a double-layer combination of positive and lift-off resist. The smallest feature (barber pole line) was 0.7 μm in size and the positioning was better than 50 nm (nominal). A detailed picture of the bridges in the final design for a cassette tape array is shown in Fig. 9.

The fabrication tolerances and design rules described above accounted for arrays with less than 5% of variation in

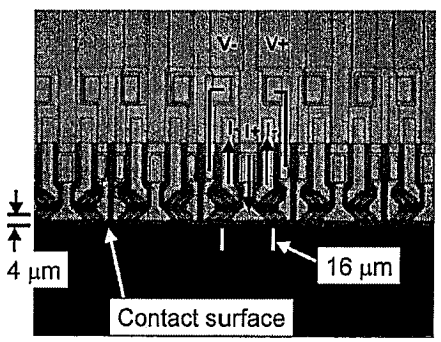

FIG. 9. Photograph of the finished cassette tape (4 mm wide) imaging array, zoomed in on several of the bridges. The current and voltage taps are shown for one bridge.

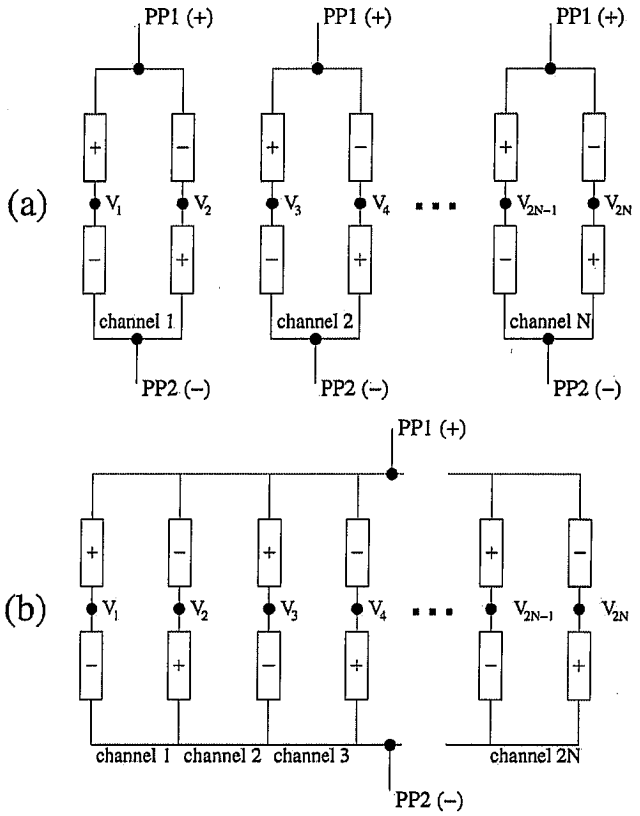

FIG. 10. Schematic diagram of the (a) full-step bridge and (b) half-step bridge configurations.

the element resistance and 16 bit dynamic range at 8 kscans/s. These results were obtained by measuring bridge offset from the transfer curves of all elements in the array.

IV. ELECTRONICS MODULE

The sensing cell described in Fig. 7(c) has a 32 μm long footprint (96 μm for the video tape head) and individually represents one channel. The schematic diagram of this full-step bridge is shown in Fig. 10(a) and the voltage of each channel i, $V_{\mathrm{ch}\,i}$ is given by

$$V_{\mathrm{ch}i} = V_{2i} - V_{2i-1}, \tag{1}$$

where $1 \leqslant i \leqslant N$ and N is the total number of bridges.

With the same number of bridges, we can measure twice as many channels by using an interleaved or half-step bridge configuration shown in Fig. 10(b). The voltage of each channel is now given by

$$V_{\mathrm{ch}i} = (-1)^i (V_i - V_{i-1}). \tag{2}$$

Here, $V_{\mathrm{ch}\,0} \equiv 0$ and therefore $V_{\mathrm{ch}\,1} = V_1$. Equation (2) describes a system of $2N$ linear equations and $2N$ unknowns. The system is computationally fast to solve because it involves only additive operations provided that there is no cross-talk between the channels. One source of electrical cross-talk is the resistance between the power planes and the bridge sensing elements. However, resistance network simulations showed that if the power plane resistance is less than 0.1 Ω the cross-talk decreases to the same levels of the sensing element noise floor. All barber pole lines, power planes, and voltage connections were therefore fabricated using Al as a connecting metal.

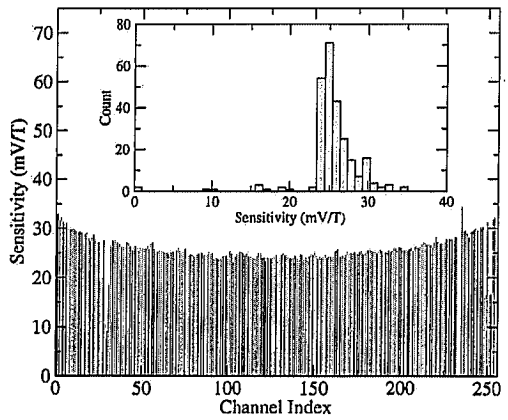

FIG. 11. Magnetic field sensitivity of the elements in the sensor array and the corresponding sensitivity histogram (inset).

Figure 11 shows the sensitivity of each element in the array with respect to the sensor index. The sensitivity is defined as the slope of the straight line that interpolates the sensor response to the magnetic field in the linear regime and is reported here in mV/T units. A histogram (Fig. 11 inset) shows that 80% of the sensitivities are within one standard deviation from the average of 25.5 mV/T with the exception of a few channels that were saturated. These affected channels were 2%–3% of the total number of channels. An estimate of the magnetic field for these channels is approximated by the averaging of the adjacent channels. Figure 11 also shows that the nonuniformities in the sensitivities are systematic and symmetric. This systematic symmetry is a consequence of inhomogeneities in the calibration field or in the current distribution across the bridges which changes the current-induced bias in the barber poles.[5] The sensitivity data are used to calibrate the magnetic field measurements of each sensor and therefore provide a uniform linear response of the array.

The interface between the sensor array channels and the electronics module shown in Fig. 12 describes the signal path from bridges in the sensor array to the acquisition cards placed in the host computer. The electronics consists of a socket board to isolate the different channels, a multiplexer board that serves to preamplify the signals and multiplex them onto 32 (16 differential pairs) channels, and a filter

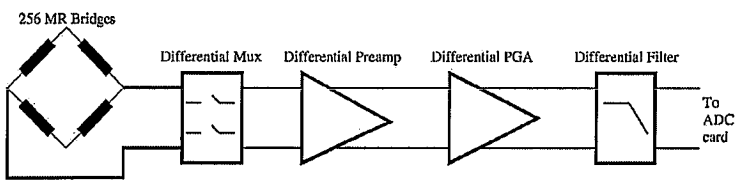

FIG. 12. Diagram showing the flow of the signal through the electronics module.

board where they are further amplified and the high frequency components are removed. The filter board outputs the 32 channels of signal to the two analog-input data acquisition boards. The filter board also provides power to the sensor array and the connections to the host computer are made using standard 68-pin SCSI connectors.

The socket board is an eight-layer board with a custom socket designed to hold a single 13×13 mm^2 die containing the 256 element magnetoresistive array and the test structures. The output pads for the 256 differential signals are in an 18×18 pad matrix with 600 μm by 700 μm spacing. The extra pads are used for bias current. The die is loaded into the socket with the pads facing down so that they will make contact with the spring-loaded (pogo) pins and the array stripe aligned with the opening in the socket. These pins interface with pads on the board where the 256 differential channels are broken out. Connection to the multiplexer board is through four 4×21 connectors with 2 mm spacing.

The multiplexer board is the first stage of signal processing. The 256 differential channels are fed into 16 differential multiplexers. The multiplexed differential voltages, which follow Eq. (2), provide the input to the preamplifier stage. Four lines of digital output from a high speed digital input/output card are programmed to step through the multiplexers in the correct order. High precision, low noise operational amplifiers, used in a differential configuration, move the signal level away from the noise floor. The multiplexer board sends the differential channels to the filter board that is inside the electronics enclosure through a 68 conductor ribbon cable. We found that the time to settle at the preamplifier stage is close to 2 μs for a voltage swing of 50 mV.

The filter board takes in the differential voltages, amplifies the signal with a high speed, programmable gain instrumentation amplifier where the gain is programmed with two channels of the high speed digital input/output card. This feature maintains the maximum dynamic range into the analog-to-digital converters on the input cards. The final signal processing stage is a differential Sallen-Key filter[9] with a roll off near 300 kHz.

The differential output of the Sallen-Key filter is then sent to a data acquisition card where the signals are digitized and processed further in software. The acquisition cards read eight channels of differential analog signals at a sampling rate of 25 ksamples/s which represents an aggregate sampling bandwidth of 200 kHz. The average cassette tape speed is approximately 5 cm/s. At 25 ksamples/s, each scan is spatially separated by 2 μm. This is the real-time spatial resolution of the magnetic imaging system. Finally for a voltage swing of 2 V a settling time of less than 4 μs can be achieved which is equivalent to a 250 kHz maximum sampling bandwidth.

The filter board also contains the current source for the bridges and the power regulating electronics. Further conditioning is provided at the point-of-load regulators on the multiplexer board. All differential signal traces on the three boards have minimum pickup loops to reduce external noise. Analog and digital ground planes are kept separate and all connecting cables are arranged to isolate digital lines from analog lines. The potentiometer on the front of the electronics enclosure regulates the current driving the sensing bridges.

After the signal from the bridges is converted into a 16 bit digital format, the host computer organizes the information and displays each channel as a horizontal trace where the shade of gray defines the amplitude of the signal (black and white for a saturated negative and positive signal) in the time domain (horizontal axis.)

V. SOFTWARE

The software interface combines four main modules that help the operator configure and calibrate the hardware, acquire, and analyze images. The modules names are *calibration, player controls, plotting*, and *important variables*. In the calibration module, set points for the bridge voltage and channel amplifier gain are entered. In addition, operating parameters such as sensitivity and bridge offset for each channel are measured and stored.

The player controls module helps the operator adjust the home positions of the head for the image scan acquisition. A virtual tape deck with the "play," "stop," "pause," "fast forward," and "rewind" buttons assists the operator in imaging the relevant sections of the tape for the analysis. Here, when the play button is pressed, the acquisition window opens to show, in real time, the acquired image scan as the corresponding audio is played. The new window controls the play volume and has basic image manipulation and data extraction functionalities that help the operator isolate and characterize, *in situ*, the recently acquired image.

A more detailed and comprehensive set of image manipulation and data analysis functions are present in the plotting module (Fig. 13) for the analysis of current or previously acquired scans. In this module, the operator can switch to other modules via the module tab bar [Fig. 13(a)] and turn on and off the application window in the main control toolbar [Fig. 13(b)]. The image manipulation toolbar [Fig. 13(c)] can read and save previously acquired scans, zoom into a specific area of the image or visualize the entire scan, and change the color palette and contrast of the image. The data manipulation toolbar [Fig. 13(f)] manages four analysis tools. The first, shown in the image window, is a two-dimensional color map of the cross track versus downtrack field amplitude called the image window. In the image window shown in Fig. 13(d) a gray scale shows negative field values pointing toward black and positive field values pointing toward white. The second is the channel downtrack scan line, a two-dimensional plot [Fig. 13(e)] showing the amplitude of the magnetic field measured by a single channel selected via a horizontal dotted line in the image window. The cross-track scan line [Fig. 13(g)] provides the magnetic field measured as a function of the channel index in the direction perpendicular to the tape movement. A vertical dotted line assists the operator in selecting the position for the cross-track line scan. Finally, the average scan tool performs a spatial average of the cross-track data bound by two horizon-

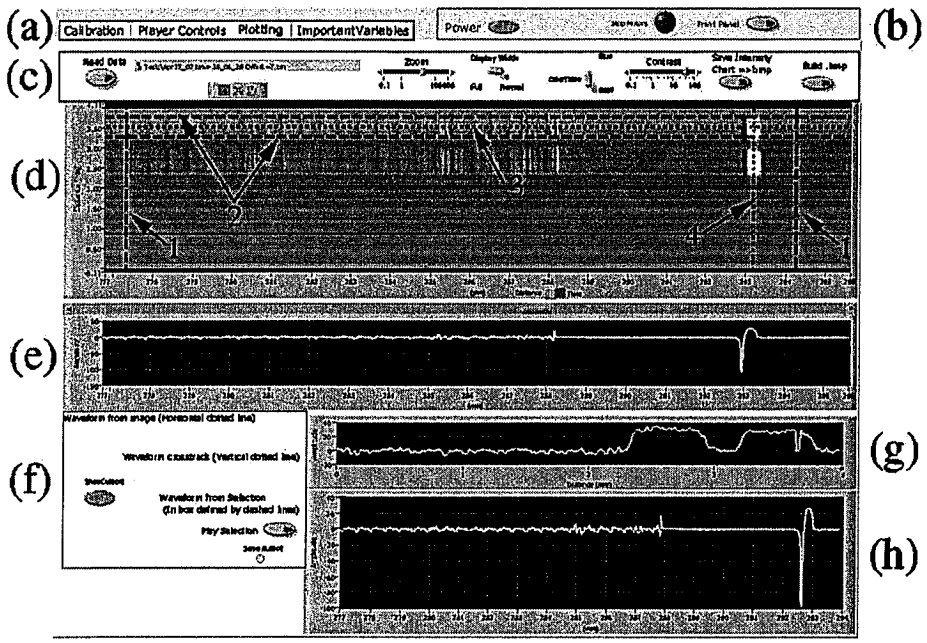

FIG. 13. (Color online) Screenshot of the software interface in the plotting module where we can see (a) the module tabs; (b) the main control toolbar; (c) the image manipulation toolbar; (d) the image window: (1) the average scan horizontal delimiter lines, (2) the average scan horizontal delimiter lines, (3) the channel downtrack scan line, (4) the cross-track scan line; (e) the individual channel downtrack scan window; (f) the data manipulation toolbar; (g) the cross-track scan window; and (h) the downtrack average scan window.

tal dashed lines in the image window. The average is plotted [Fig. 13(h)] as a function of the position in a range defined by two vertical dashed lines.

VI. APPLICATIONS

Figure 14 shows the image of an audio tape obtained by the audio tape head. The image focuses on one of the sides where an audio signal was previously recorded. The audio was partially erased by the same recording head and characteristic mark was left when the recording head was removed. In forensic analysis the head stop mark is an indication that the tape was altered and helps determine the validity of the evidence.

The important aspect of this image is that it was taken while the tape was being played. The captured event was triggered by the operator when the discontinuity was heard. In addition, the software allows the operator to play back the signal from any given selection of the tape. This is a powerful new addition to the tape forensics toolbox. Finally, it is possible to digitally image the entire tape. Given a storage requirement of 8 Mbyte of data per second of audio, it would require only 43 Gbytes to store the image of a typical 90 min tape.

Figure 15(a) shows a 1 s scan of a cassette tape imaged with the 256-channel sensor array. At the bottom half of the scan the figure shows three regions. Region I shows the typical image signature of a stereo audio pattern. The audio was erased in region II where a sharp interface marks the start of an erase head event. Region III highlights the erase head stop event. Figure 15(b) shows in detail the erase stop event measured with the sensor array in comparison to the same section imaged using the Bitter technique [Fig. 15(c)]. The erase stop event has a magnetic pattern that is unique for each type of tape recorder (brand and model) and can be seen in more detail by the 256-sensor array.

Figure 16 shows the image of a video tape where we can see the stereo audio traces at the bottom, the video signal covering most of the image in the middle, and the synchronization marks at the top. The gray scale follows the polarity of the field so that black and white represent the saturation state of the sensor in opposite directions, respectively. Both audio channels could be recovered by simply converting the image digital data into an analog signal output to a speaker. These images are acquired as the examiner views and listens to the tape. Again, the acquisition stops when an event is seen on the scan or heard by the examiner.

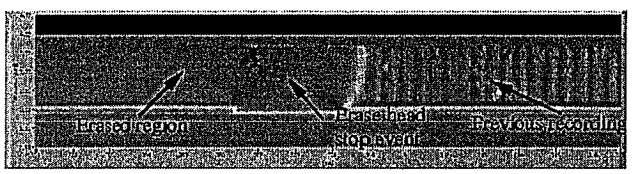

FIG. 14. Image of an audio tape obtained with the audio tape head.

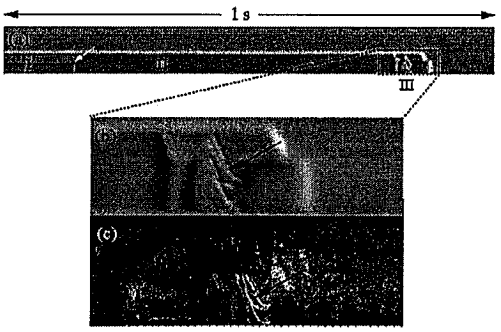

FIG. 15. (a) 1 s of audio in a cassette tape imaged using the 256-sensor array: (I) regular audio signature, (II) erased region, and (III) erase head stop event. The white arrow indicates the erase mark starting point. The dotted rectangle highlights the erase stop event showed in detail in (b) and compared with the Bitter technique (c). The black arrows indicate the recorder signature marks.

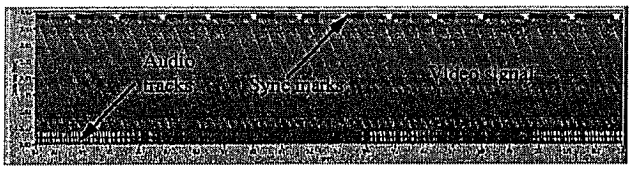

FIG. 16. 1 s of video in a video tape obtained with the 256-sensor array.

VII. SUMMARY

We have demonstrated a system that is capable of imaging magnetic tapes in real time during tape reproduction. The system operates with an array of 256 AMR barber pole sensors. A thorough description of the system provided in this paper shows how reliable the system can be in imaging magnetic tapes for forensic purposes. Other potential applications of the system include current mapping of printed circuit boards and semiconductor chips, stress and fracture analysis, and magnetic bead sensing for biological systems. One audio tape imaging system unit has been delivered to the Federal Bureau of Investigation and is currently being validated for use in authentication of evidence for forensic investigation purposes.

ACKNOWLEDGMENTS

We would like to thank Ken Marr and the support given by the Federal Bureau of Investigation Quantico Audio Laboratory, the Department of Justice, the National Institute of Standards and Technology office of Law Enforcement Standard and Magnetics Competence Program, and Stephen E. Russek for his assistance and advice.

[1] B. E. Koenig, J. Audio Eng. Soc. **38**, 3 (1990).
[2] N. H. Yeh, IEEE Trans. Magn. **16**, 979 (1980).
[3] D. P. Pappas, A. V. Nazrov, D. Stevenson, S. Voran, M. E. Read, E. M. Gormley, J. Cash, K. Marr, and J. J. Ryan, J. Electron. Imaging **14**, 013015 (2005).
[4] S. T. Halloran, F. C. S. da Silva, H. Z. Fardi, and D. P. Pappas, J. Appl. Phys. **102**, 033904 (2007).
[5] S. Tumanski, *Thin Film Magnetoresistive Sensors* (IOP, Bristol, 2001), pp. 22–70.
[6] S.-J. Han, L. Xu, H. Yu, R. J. Wilson, R. L. White, N. Pourmand, and S. X. Wang, 2006 International Electron Devices Meeting, 2006 (unpublished).
[7] D. Wang, J. Daughton, C. Nordman, P. Eames, and J. Fink, J. Appl. Phys. **99**, 08H703 (2006).
[8] See, for example, J. Nogues and I. K. Schuller, J. Magn. Magn. Mater. **192**, 203 (1999).
[9] See, for example, P. Horowitz and W. Hill, *The Art of Electronics* (Cambridge University Press, Cambridge, 1989), p. 267.